Electric Power Systems Research 103 (2013) 49–60

Contents lists available at SciVerse ScienceDirect

Electric Power Systems Research

journal homepage: www.elsevier.com/locate/epsr

Control of a wind generation system based on a Brushless Doubly-Fed Induction Generator fed by a matrix converter

Roberto Cárdenas[a,*], Rubén Peña[b], Patrick Wheeler[c], Jon Clare[c], Andrés Muñoz[d], Alvaro Sureda[d]

[a] University of Chile, Department of Electrical Engineering, Santiago, Chile
[b] University of Concepcion, Department of Electrical Engineering, Concepcion, Chile
[c] University of Nottingham, Department of Electrical and Electronic Engineering, Nottingham University Park, NG7, 2RD, Nottingham, England, UK
[d] University of Santiago de Chile, Department of Electrical Engineering, Chile

ARTICLE INFO

Article history:
Received 30 October 2012
Received in revised form 2 March 2013
Accepted 9 April 2013
Available online 7 June 2013

Keywords:
Variable speed wind energy generation
Brushless Doubly-Fed Induction Machines
Matrix converters

ABSTRACT

The Doubly-Fed Induction Generator (DFIG) is one of the most widely used generators for wind energy applications with more than 50% of installed Wind Energy Conversion Systems (WECS) using this variable speed technology. However, the conventional DFIG requires brushes and copper slip-rings to connect a power converter to the rotor windings. The use of brushes decreases the WECS' robustness and extra maintenance is required to periodically inspect/replace these elements. In this work a new topology for a Brushless Doubly-Fed Induction Generator (BDFIG) is presented. As an alternative to conventional Voltage Source Inverters (VSI) a matrix converter is used to regulate the current supplied to the stator of the doubly-fed machine, supplying the excitation energy to the WECS. The proposed generation system is mathematically analysed in this paper and the design of the control loops is discussed. Because the power spectrum density of the wind speed is dominated by low frequency components, in this work some simplifications of the transfer functions of the system are proposed. Experimental results obtained from a 3 kW prototype of a cascaded DFIG, are presented and fully discussed.

1. Introduction

The Doubly-Fed Induction Generator (DFIG) is one of the most widely used generators for wind energy applications with more than 50% of installed Wind Energy Conversion Systems (WECS) using this variable speed technology [1]. However, the conventional DFIG requires brushes for connecting a converter to the rotor windings. As has been highlighted in several publications, the use of brushes decrease the WECS robustness and extra maintenance is required in order to periodically replace these elements.

The Brushless Doubly Fed Induction Generator (BDFIG) has emerged as a suitable alternative to the DFIG for grid connected and stand-alone applications [2–4]. The main advantage of this machine is the lack of brushes with consequently reduced maintenance. This is certainly a desirable characteristic, particularly for wind turbines located in remote areas such as in off-shore applications.

The BDFIG was reported in the literature by Hunt and Creedy in the early years of the 20th century [5–7]. Some basic aspects of the BDFIG were also discussed in 1967 [8]. The first implementations of BDFIGs used two Doubly-Fed Induction Machines (DFIMs) affixed to the same shaft with their rotor windings connected. This topology is known as the Cascaded BDFIG [5,6,8–13] (see Fig. 1a) and was used in the early days for frequency conversion and for adding slip resistances to the main machine without using brushes [5,6]. In the cascaded BDFIG one of the DFIM is the power machine and its stator is connected to the grid. The other DFIM is the excitation machine and its stator is connected to the grid through a bidirectional power converter.

An improvement to the implementation of cascaded DFIGs is the "self-cascaded" BDFIG which is reported in [9,14,15]. In this machine two separate windings are located on the stator, sharing the same magnetic circuit. The stator windings have different numbers of poles to avoid direct coupling between them. The rotor is designed to couple with both stator windings [16–19]. The main advantage of this topology is that only one machine, with two stators, is required instead of two machines affixed to the same shaft

* Corresponding author at: University of Chile, Avenida Tupper 2007, Postcode 8370451, Chile. Tel.: +56 2 9784816; fax: +56 2 6720162.
E-mail addresses: rcardenas@ing.uchile.cl, rcd@ieee.org (R. Cárdenas), rupena@udec.cl (R. Peña), pat.wheeler@nottingham.ac.uk (P. Wheeler), jon.clare@nottingham.ac.uk (J. Clare).

0378-7796/$ – see front matter © 2013 Elsevier B.V. All rights reserved.
http://dx.doi.org/10.1016/j.epsr.2013.04.006

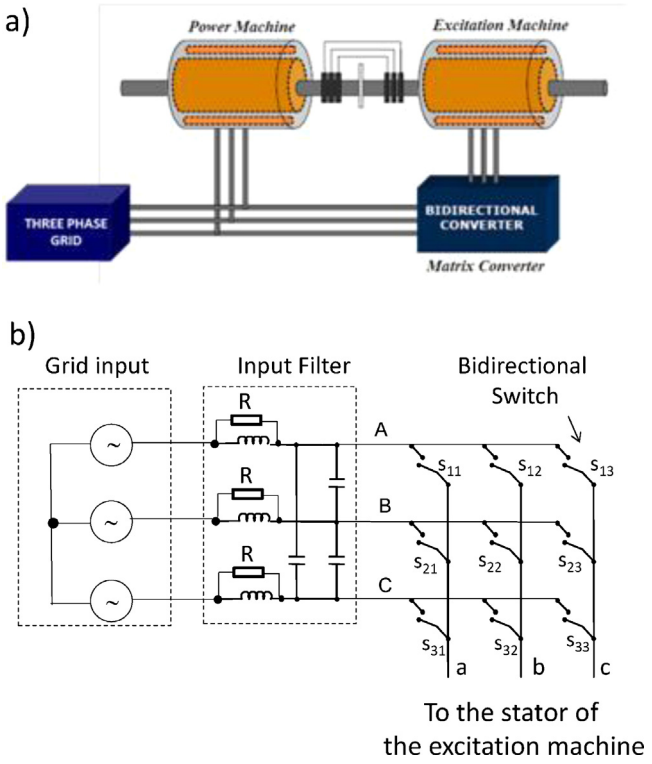

Fig. 1. (a) BDFIG based on a cascaded topology and (b) 3×3 MC used in this work.

(see Fig. 1). In the "self-cascaded" BDFIG one of the stator windings is for excitation purposes and the other is connected to the grid.

Vector control of the BDFIG has been proposed in [4,12,18,20–23]. In these papers it is proposed to use back-to-back converters (as a bidirectional converter) which are rated at only a fraction of the nominal power [22,25]. This is similar to the rating of the power converters required in a conventional DFIG, which are usually designed for 30% of the DFIG's nominal power [26,27]. Wind energy applications of BDFIGs have also been discussed by a number of researchers in [3,4,28–31]. However in previous papers relating to the applications of BDFIGs in WECs, only simulations are reported. A detailed analysis of the control system design has not been presented in these publications.

In this paper a new topology fora BDFIG system is proposed. It is based on a 3×3 Matrix Converter (MC) which replaces the back-to-back voltage source converter used in [20–23]. The typical components of a 3×3 MC are shown in Fig. 1b. The main advantages of a matrix converter are its high power to mass and power to volume ratios [32–35]. A detailed comparison between MCs and back to back voltage source converters is presented in [35]. It is shown in that publication that, depending on the switching frequency of the IGBT devices, the power to volume ratio of the MC is between 3.5 and 10 times higher than that of a corresponding back-to-back power converter. Additionally, the power to mass ratio is about 5 times higher for the MC with respect to that of a back-to-back voltage source inverter. Furthermore, it is also reported in [35] that, depending on the switching frequency, the volume of the passive components, e.g. EMI input filter and the heat sink, are much smaller in the MC when compared with an equivalent back-to-back power converter. An additional advantage is that the MC can be embedded in the stator of the excitation machine [36]. Therefore the main advantages of the matrix converter are in the compactness and reliability of the converter.

The contributions of this paper are not only related to the application of MCs to BDFIGs [24]. In wind energy applications, most of the power spectrum density is in the low frequency region. This allows some substantial simplifications to the modelling and control of the BDFIG. In this paper, a control system based on two nested current control loops is proposed for the control of the BDFIG in wind energy applications. The fast inner control loop regulates the d–q axis currents of the excitation machine. The slower outer control loops regulate the d–q currents in the grid-connected machine. It is shown that by using sensible assumptions, simplified transfer functions can be obtained for the design of the current controllers. The performance of the generation system, for wind energy applications, is discussed and experimentally demonstrated. A wind turbine of variable size and power is emulated using a third machine affixed to the common shaft and speed-controlled using a commercial inverter. Real wind profiles obtained from the Rutherford Appleton Laboratories (Oxford UK) are used to test the performance of the proposed WECS. A DSP platform is used for control purposes.

The rest of this paper is organised as follows. In Section 2 the proposed modelling of the BDFIG for wind energy applications is discussed. In Section 3 the control systems are presented and extensively discussed. In Section 4 the MC topology and control systems are briefly reviewed. In Section 5 experimental results are discussed. Finally Section 6 presents the conclusions.

Because of the experimental facilities available in the power electronics and machine lab where this system was implemented, a cascaded BDFIG is used to validate the proposed control systems. However, because of the similarities in the modelling and control of cascaded and self-cascaded machines, this experimental validation is considered sufficient to validate the performance of the proposed control system to both topologies of BDFIGs.

2. Modelling of the Brushless DFIG

The model used in this work is based on the single-phase diagram shown in Fig. 2. Each machine is represented by its rotor resistance, stator resistance, magnetising inductance and leakage inductance. The grid-connected machine is shown at the right of Fig. 2 and the excitation machine is shown at the left. The matrix converter (see Fig. 1b) is connected to the grid on its input side and the stator of the excitation machine on its output side.

The stator and rotor inductances of the two machines are defined as:

$$\begin{aligned} L_{sc} &= L_{0c} + L_{sc\sigma} \\ L_{sg} &= L_{0g} + L_{sg\sigma} \\ L_{rc} &= L_{0c} + L_{rc\sigma} \\ L_{rg} &= L_{0g} + L_{rg\sigma} \end{aligned} \tag{1}$$

The subscripts "sg", "rg" are used to indicate a variable related to the stator/rotor of the power DFIG (which is connected to the grid). On the other hand, subscripts "sc", "rc" are used to indicate a variable related to the stator/rotor of the excitation DFIG (whose stator is fed from the matrix converter output). In (1) L_{0c} and L_{0g} are the magnetising inductances of the machines, $L_{sc\sigma}$, $L_{rc\sigma}$, $L_{sg\sigma}$ and $L_{rg\sigma}$ are the stator/rotor leakage inductances of the machines.

Using α–β coordinates, the machine equations are:

$$\bar{v}_{sg} = R_{sg}\bar{i}_{sg} + \frac{d\bar{\psi}_{sg}}{dt} \tag{2}$$

$$0 = R_T\bar{i}_r + \frac{d(\bar{\psi}_{rg} - \bar{\psi}_{rc})}{dt} \tag{3}$$

$$\bar{v}_{sc} = R_{sc}\bar{i}_{sc} + \frac{d\bar{\psi}_{sc}}{dt} \tag{4}$$

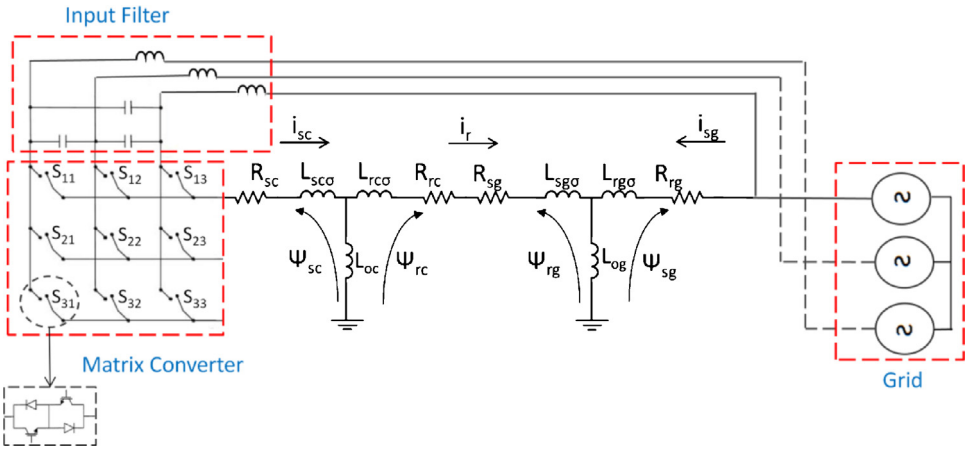

Fig. 2. Modelling of the system.

The α–β coordinates of (2), (4) are stationary and the α–β coordinates of (3) are affixed to the machine rotor. $\bar{v}_{sg}$ and $\bar{v}_{sc}$ are the voltage vectors applied to the stators of the excitation and power machines. The terms R_s and R_r stand for stator and rotor resistances respectively and R_T is defined as $R_T = R_{rc} + R_{rg}$. The symbols $\bar{\psi}_s$ and $\bar{\psi}_r$ stand for stator and rotor flux vectors.

The angular frequencies of the signals applied to the stators of the power and excitation machines are ω_{eg}, ω_{ec} respectively. It is relatively simple to demonstrate that the frequency of the signals applied to the rotor can be calculated as [16]:

$$\omega_{sL} = \omega_{ec} + p_c\omega_r = \omega_{eg} - p_g\omega_r \tag{5}$$

where p_g and p_c are the pole pair number of the grid-connected and control machines respectively. From (5), in steady state the electrical frequency of the signals applied to the stator of the excitation machines is:

$$\omega_{ec} = \omega_{eg} - (p_g + p_c)\omega_r \tag{6}$$

using a synchronous rotating frame aligned with the stator flux of the grid-connected DFIG, the d–q model of the system is obtained as:

$$\bar{v}_{sg} = R_{sg}\bar{i}_{sg} + \frac{d\bar{\psi}_{sg}}{dt} + j\omega_{eg}\bar{\psi}_{sg} \tag{7}$$

$$0 = R_T\bar{i}_r + \frac{d(\bar{\psi}_{rg} - \bar{\psi}_{rc})}{dt} + j(\omega_{eg} - p_g\omega_r)(\bar{\psi}_{rg} - \bar{\psi}_{rc}) \tag{8}$$

$$\bar{v}_{sc} = R_{sc}\bar{i}_{sc} + \frac{d\bar{\psi}_{sc}}{dt} + j(\omega_{eg} - (p_c + p_g)\omega_r)\bar{\psi}_{sc} \tag{9}$$

The fluxes $\bar{\psi}_s$ and $\bar{\psi}_r$ are defined as:

$$\bar{\psi}_{sg} = L_{sg}\bar{i}_{sg} + L_{0g}\bar{i}_r \tag{10}$$

$$\bar{\psi}_{sc} = L_{sc}\bar{i}_{sc} - L_{0c}\bar{i}_r \tag{11}$$

$$\bar{\psi}_{rg} = L_{rg}\bar{i}_r + L_{0g}\bar{i}_{sg} \tag{12}$$

$$\bar{\psi}_{rc} = -L_{rc}\bar{i}_r + L_{0c}\bar{i}_{sc} \tag{13}$$

Additionally $\bar{\psi}_r$ is defined as:

$$\bar{\psi}_r = (\bar{\psi}_{rg} - \bar{\psi}_{rc}) = L_{0g}\bar{i}_{sg} - L_{0c}\bar{i}_{sc} + L_r\bar{i}_r \tag{14}$$

where $L_r = L_{rg} + L_{rc}$. The current vector $\bar{i}_r$ is calculated from (14) as:

$$\bar{i}_r = \frac{\bar{\psi}_{sg} - L_{sg}\bar{i}_{sg}}{L_{0g}} \tag{15}$$

defining $\omega_{sl} = (\omega_{eg} - p_g\omega_r)$ and replacing (12)–(15) in (8) yields:

$$0 = [sL_r + R_T + j\omega_{sl}L_r]\bar{\psi}_{sg} + [s(L_{0g}^2 - L_rL_{sg}) - R_TL_{sg} + j\omega_{sl}(L_{0g}^2 - L_rL_{sg})]\bar{i}_{sg} - [L_{0c}L_{0g}(s + j\omega_{sl})]\bar{i}_{sc} \tag{16}$$

where "s" is the Laplace operator. From (16) and considering that the flux $\bar{\psi}_{sg}$ is almost constant (because the proposed generation system is grid connected) a small signal model is obtained as:

$$\frac{\Delta\bar{i}_{sg}}{\Delta\bar{i}_{sc}} = \frac{L_{0c}L_{0g}(s + j\omega_{sl})}{s(L_{0g}^2 - L_rL_{sg}) - R_TL_{sg} + j\omega_{sl}(L_{0g}^2 - L_rL_{sg})} \tag{17}$$

The transfer function of (17) can be divided into its real and imaginary components using standard operations for complex fractions. After some manipulation and defining:

$$\sigma L = (L_rL_{sg} - L_{0g}^2) \tag{18}$$

it can be shown that the transfer function of (17) can be obtained as:

$$\frac{\Delta\bar{i}_{sg}}{\Delta\bar{i}_{sc}} = G_d(s) + jG_q(s) \tag{19}$$

where the "direct" transfer function $G_d(s)$ is defined as:

$$G_d(s) = \frac{-L_{0c}L_{0g}(s^2 + (R_TL_{sg}/\sigma L)s + \omega_{sl}^2)}{\sigma L(s^2 + 2(R_TL_{sg}/\sigma L)s + (R_TL_{sg}/\sigma L)^2 + \omega_{sl}^2)} \tag{20}$$

and the "quadrature" transfer function is defined as:

$$G_q(s) = -\frac{L_{0c}L_{0g}R_TL_{sg}}{\sigma L^2}\frac{\omega_{sl}}{(s^2 + 2(R_TL_{sg}/\sigma L)s + (R_TL_{sg}/\sigma L)^2 + \omega_{sl}^2)} \tag{21}$$

The quadrature transfer function represents the cross-coupling between the d-axis and q-axis components of the stator currents. The d–q components of the current vector $\Delta\bar{i}_{sg}$ can be obtained from (19) as:

$$\begin{bmatrix}\Delta i_{sgd}\\ \Delta i_{sgq}\end{bmatrix} = \begin{bmatrix}G_d(s) & -G_q(s)\\ G_q(s) & G_d(s)\end{bmatrix}\begin{bmatrix}\Delta i_{scd}\\ \Delta i_{scq}\end{bmatrix} \tag{22}$$

In Fig. 3 the Bode diagrams of $G_d(s)$ are shown, while Fig. 3a shows the magnitude. In the low frequency range, below 10 Hz, the magnitude is fairly constant with a phase angle of $\approx 180^\circ$ (see Fig. 3b). In Fig. 4, the Bode diagrams of $jG_q(s)$ are shown. In this case the magnitude is also fairly constant in the low frequency range with a phase angle of $\approx -90^\circ$.

The transfer functions of (20)–(21) are strongly dependant on the value of the slip frequency ω_{sl} which is rather large for the

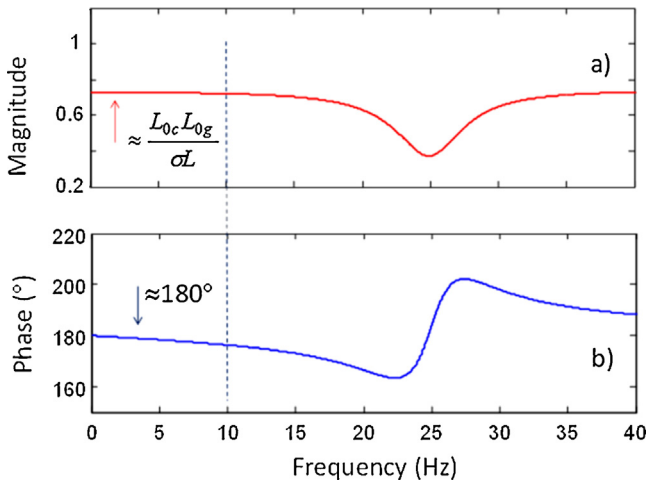

Fig. 3. Bode diagrams corresponding to the magnitude and angle of $G_d(s)$. (a) Magnitude and (b) angle.

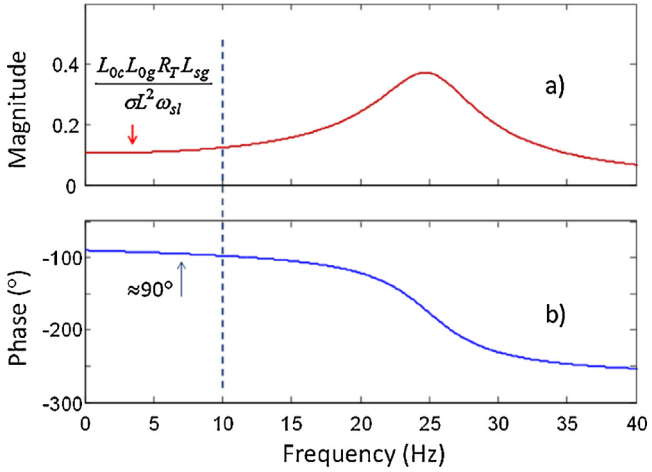

Fig. 4. Bode diagrams corresponding to the magnitude and angle of $jG_q(s)$. (a) Magnitude and (b) angle.

BDFIG (because $\omega_{sl}=(\omega_{eg}-p_g\omega_r)$). For instance in steady state the magnitude of $G_q(s)$ is inversely proportional to the slip and the value $G_q(0)$ is relatively small.

Figs. 3 and 4 have been obtained considering the parameters of the experimental rig (see Appendix) and a rotational speed of $\omega_r=750$ rpm. Considering that the experimental system has been implemented with 4-pole DFIGs, the value of ω_{sl} in (20)–(21) for $\omega_r=750$ rpm is of 157.07 (electrical) rad s^{-1}. The value of $G_q(0)$ is proportional to the rotor resistance R_T (see (21)) which is small in large machines in order to reduce copper losses. Therefore in large machines a lower value of cross-coupling is expected between the d–q axis currents (see (22)).

3. Proposed control system

3.1. Control of the stator current in the excitation machine

The stator of the excitation machine is fed from the MC output. The stator voltage $\bar{v}_{sc}$ is obtained from (9). Replacing (11), (15) in (9) and assuming that the flux $\bar{\psi}_{sg}$ is constant and the dynamics of the current are faster than the speed dynamics, the transfer function $\overline{\Delta v}_{sc}/\overline{\Delta i}_{sc}$ is:

$$\overline{\Delta v}_{sc}=(R_{sc}+sL_{sc}+j\omega_{ec}L_{sc})\overline{\Delta i}_{sc}+\frac{L_{0c}L_{sg}}{L_{0g}}(s+j\omega_{ec})\overline{\Delta i}_{sg} \tag{23}$$

where ω_{ec} is defined as $\omega_{ec}=(\omega_{eg}-(p_c+p_g)\omega_r)$. Using (19), (22) in (23), yields:

$$\overline{\Delta v}_{sc}=(R_{sc}+sL_{sc}+j\omega_{ec}L_{sc})\overline{\Delta i}_{sc}+\frac{L_{0c}L_{sg}}{L_{0g}}(s+j\omega_{ec})(G_d(s)+jG_q(s))\overline{\Delta i}_{sc} \tag{24}$$

For wind energy applications, relatively low frequency components are expected in the current $\overline{\Delta i}_{sc}$. Therefore, the low frequency evaluations of $G_d(s)$ and $G_q(s)$ are considered in (24) (see Figs. 3 and 4). With this simplification the transfer function $\overline{\Delta v}_{sc}/\bar{i}_{sc}$ is obtained as:

$$\frac{\overline{\Delta v}_{sc}}{\overline{\Delta i}_{sc}}= \left(R_{sc}-\omega_{ec}G_{q0}(s)\frac{L_{0c}L_{sg}}{L_{0g}}\right)+s\left(L_{sc}+\frac{L_{0c}L_{sg}}{L_{0g}}G_{d0}(s)\right) +j\omega_{ec}\left(L_{sc}+\frac{L_{0c}L_{sg}}{L_{0g}}G_{d0}(s)+s\frac{L_{0c}L_{sg}}{\omega_{ec}L_{0g}}G_{q0}(s)\right) \tag{25}$$

From (25) the following terms are defined:

$$R_{eq}=\left(R_{sc}-\frac{L_{0c}L_{sg}}{L_{0g}}\omega_{ec}G_{q0}(s)\right) \tag{26}$$

$$L_{eq}=\left(L_{sc}+\frac{L_{0c}L_{sg}}{L_{0g}}G_{d0}(s)\right) \tag{27}$$

Neglecting the term $sG_q(0)$ in (25) the following expression is obtained:

$$\frac{\overline{\Delta v}_{sc}}{\overline{\Delta i}_{sc}}\approx(R_{eq}+sL_{eq})+j\omega_{ec}L_{eq} \tag{28}$$

This expression is similar to that used to control a standard DFIG [1]. The transfer function considers the effects of the equivalent resistance, the equivalent inductance and a cross-coupling term. The design of the current controllers is straightforward and is addressed in Section 3.3 below.

3.2. Tracking of the wind turbine maximum power point

As is well known, the frequencies of the signals applied to the stator and rotor of an induction machine are related by the slip coefficient. If the slip coefficients of the excitation and power machine are defined as s_c and s_g respectively (see Fig. 5), the slip frequency f_{sl} is obtained as:

$$f_{sl}=s_cf_{ec}=s_gf_{eg} \tag{29}$$

Therefore the slip coefficients are obtained as:

$$s_c=\frac{f_{sl}}{f_{ec}}\quad s_g=\frac{f_{sl}}{f_{eg}} \tag{30}$$

As shown in [37], in a DFIM the stator and rotor power are related by:

$$P_{rc}\approx s_cP_{sc}\quad P_{rg}\approx s_gP_{sg} \tag{31}$$

neglecting the losses, i.e. $P_{rc}=P_{rg}$, and calculating the total output power from the BDFIG as:

$$P_{out}=(P_{sg}-P_{sc})=P_{sg}\left(1-\frac{s_g}{s_c}\right) \tag{32}$$

Using (30) in (32) and $\omega_{ec}=(\omega_{eg}-(p_c+p_g)\omega_r)$ yields:

$$P_{out}=(p_g+p_c)\frac{\omega_r}{\omega_{eg}}P_{sg} \tag{33}$$

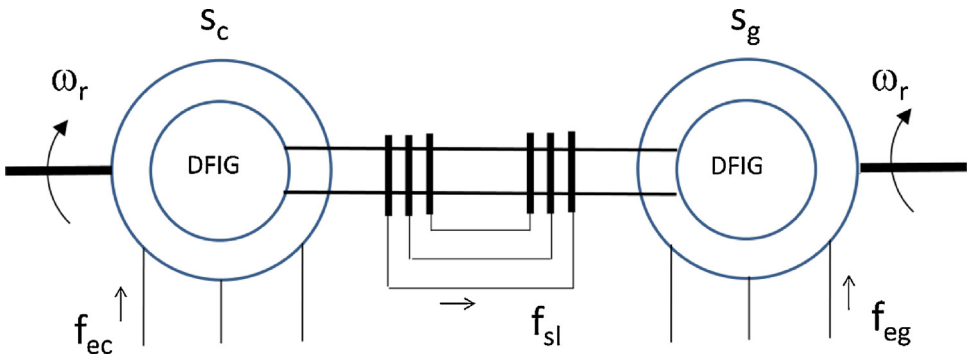

Fig. 5. Brushless generation system, showing the slip coefficients of each machine and signal frequencies in each winding.

It is well known that in a Wind Energy Conversion System (WECS) the maximum aerodynamic efficiency is obtained when the generated power is proportional to the cube of the rotational speed [32]. Therefore:

$$p_{out} = k_{opt}\omega_r^3 = (p_g + p_c)\frac{\omega_r}{\omega_{eg}}P_{sg} \tag{34}$$

where k_{opt} is dependent on the gear box ratio, blade aerodynamics, blade radius, etc. From (34) the power P_{sg} can be calculated as:

$$P_{sg} = \frac{\omega_{eg}k_{opt}}{(p_g + p_c)}\omega_r^2 = k_T\omega_r^2 \tag{35}$$

The small signal model of (35) is:

$$\Delta P_{sg}(s) = 2k_T\omega_{r0}\Delta\omega_r(s) \tag{36}$$

Additionally, the stator power can be calculated as:

$$P_{sg} = k(v_{sgd}i_{sgd} + v_{sgq}i_{sgq}) \tag{37}$$

where k depends on the current and voltage transformations used to refer from a three phase stationary frame to a two phase stationary frame. If the d-axis is orientated along the stator flux $\bar{\psi}_{sg}$ the grid voltage vector is $\bar{v}_{sg} \approx jv_{sgq}$. Therefore the small signal model of (37) is:

$$\Delta P_{sg} \approx kv_{sgq0}\Delta i_{sgq} \tag{38}$$

Using (25)–(27), (36)–(38) and the values of G_{d0}, G_{q0} obtained from (20)–(21), the linearised control system of Fig. 6 is proposed which is based on two nested loops where the internal loop is used to regulate the stator current of the excitation machine. The controller for the stator current $\bar{i}_{sc}$ is typically designed for a closed loop bandwidth (or natural frequency) between 50 Hz and 100 Hz (or more). On the other hand, the controller for the stator current $\bar{i}_{sg}$ is designed for a closed loop bandwidth of about 5–10 Hz. This relatively low bandwidth in the current $\bar{i}_{sg}$ is feasible considering that the power density in a typical wind profile is dominated by low frequency components.

As is well known, in a conventional DFIM, the power converters are designed to operate at only a fraction of the stator nominal power [27]. Using (31)–(33) it is relatively simple to demonstrate that this is also applicable to the BDFIG. From (27)–(31) and after some simple manipulations the following is obtained:

$$P_{sc} \approx \frac{s_g}{s_c}P_{sg} = \frac{\omega_{ec}}{\omega_{eg}}P_{sg} \rightarrow P_{sc} \approx \frac{\omega_{eg} - (p_g + p_c)\omega_r}{\omega_{eg}}P_{sg} \rightarrow$$
$$P_{sc} = \frac{\omega_{eg}/(p_g + p_c)\omega_r}{\omega_{eg}/(p_g + p_c)}P_{sg} = \frac{\omega_{syn} - \omega_r}{\omega_{syn}}P_{sg} = s_TP_{sg} \tag{39}$$

where ω_{syn} is the system equivalent synchronous speed [8] and s_T is defined as an overall "slip coefficient" relating the power P_{sg} to the power P_{sc}. If the rotational speed is higher than ω_{syn} power is injected into the grid from the stators of both machines, in a similar fashion to a standard DFIG (see Fig. 7 which shows super-synchronous operation). Moreover, for conventional DFIGs the operating range for the rotational speed is limited because the maximum wind power extracted from the wind is proportional to ω_r^3. Therefore, at very low rotational speed, little power capture is expected.

In this work the speed operating range of the BDFIG is limited in a similar fashion to that of a conventional DFIG. Assuming that S_T in (39) is in the range [−03 to 0.3], then the rated power of the matrix converter is 30% of the nominal stator power of the grid-connected machine. Moreover, the turns ratios of the machines have to be specified in order to match the grid and stator control machine voltage according to the operating speed range. If s_T is limited to ±30%, then the rotational speed in the experimental system used in this work is between the limits of 525 rpm and 975 rpm.

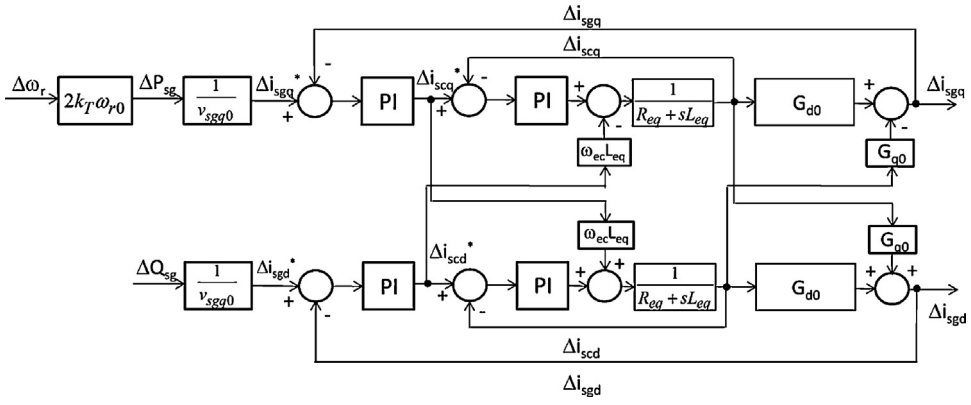

Fig. 6. Control system based on nested loops, for the proposed BDFIG.

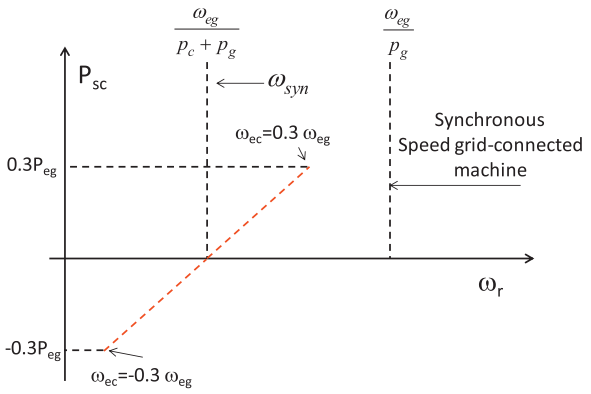

Fig. 7. Rotational speed operating range considering a S_T variation of ±30%.

Notice that the operating range of s_T also limits the frequency range of the voltages applied to the stator of the control machine. From (39) it is concluded that $\omega_{ec} \rightarrow [-0.3\omega_{eg}$ to $0.3\omega_{eg}]$. This is further explained in Fig. 7.

3.3. Design of the outer current control loop

Assuming a fast control loop for $\bar{I}_{sc}$, and assuming that the cross-coupling terms are eliminated using compensation terms (see Fig. 6), the transfer function for the design of the outer control loop corresponds to that of (20) which, for simplicity, is shown as $k_1(s^2 + a_n s + b_n)/(s^2 + a_d s + b_d)$ in Fig. 6. Therefore the open loop transfer function required for the design of the control system is:

$$G_d(s) = \frac{-L_{0c}L_{0g}(s^2 + (R_T L_{sg}/\sigma L)s + \omega_{sL}^2)}{\sigma L(s^2 + 2(R_T L_{sg}/\sigma L)s + (R_T L_{sg}/\sigma L)^2 + \omega_{sl}^2)} \quad (40)$$

Using the parameters of the experimental system, the controller design can be realised using standard design tools, for instance Evan's root locus.

The root locus for the outer control loop, considering the parameters of the experimental rig and $\omega_r = 750$ rpm is shown in Fig. 8. Notice that the transfer function of (40) is equivalent to a lead-lag network. However, the pole and zero of (40) almost cancel each other (notice that the scales of the real axis and imaginary axis in Fig. 8 are not identical). Therefore in this work they are ignored and only the dc gain of (20) (i.e. $|G_d(0)| = (L_{0c}L_{0g}/\sigma L)$) has been considered in the design of the control system for the outer loop. For the PI controller shown in Fig. 8, the damping coefficient of the dominant poles is unity. Therefore, no overshoot in the response is expected.

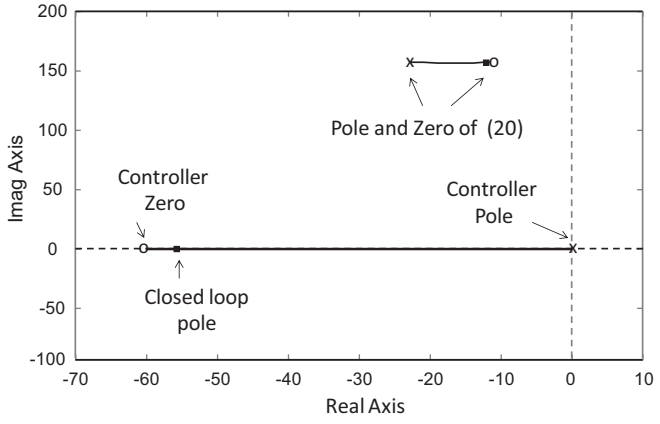

Fig. 8. Root-locus for the design of the outer current control loop.

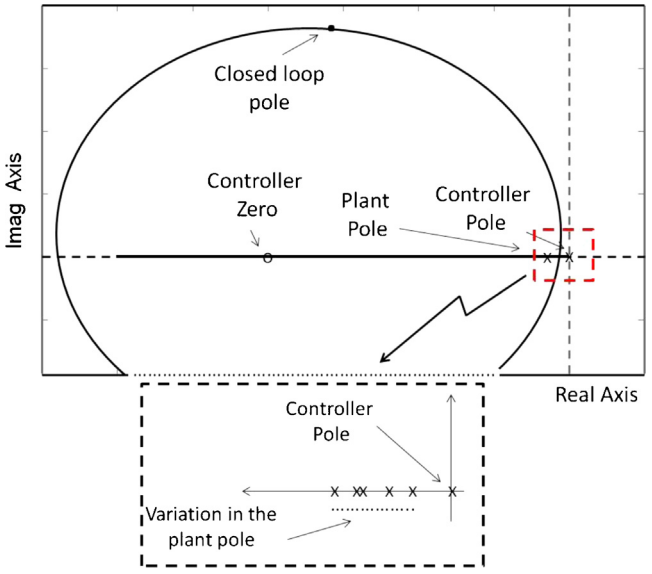

Fig. 9. Root locus for the design of the inner current control loop.

3.4. Design of the inner current control loop

The control loop for $\bar{I}_{sc}$ is designed with a bandwidth of about 10 times the bandwidth of $\bar{I}_{sg}$. Assuming that the cross-coupling terms of (28) are eliminated using decoupling terms [37], then the transfer function between the voltage and currents applied to the stator of the excitation machine is:

$$\frac{\overline{\Delta v_{sc}}}{\overline{\Delta I_{sc}}} = \frac{1}{s(L_{sc} + (L_{0c}L_{sg}/L_{0g})G_{d0}(s)) + (R_{sc} - (L_{0c}L_{sg}/L_{0g})\omega_{ec}G_{q0}(s))} = \frac{1}{sL_{eq} + R_{eq}} \quad (41)$$

The root-locus corresponding to the design of the inner loop control system is shown in Fig. 9. Notice that ω_{ec} is a variable frequency which, for a typical BDFIG, will be varying in the range of $-0.3\omega_{eg}$ to $0.3\omega_{eg}$ (see (39)). Therefore, considering the parameters of the experimental rig, the plant pole R_{eq}/L_{eq} will move from 2.2 s^{-1} to 13.4 s^{-1} (see bottom side of Fig. 9). This variation is negligible considering that the zero of the PI controller is located at $s = -200 + j0$ in the Laplace plane (for a natural frequency of $\omega_n \approx 50$ Hz). Additionally, in (41) the frequency (ω_{ec}) dependant term is multiplied by $G_{q0}(s)$ which has a small value (see Fig. 4).

The vector control system corresponding to the control diagram shown in Fig. 6, is shown in Fig. 10. The d-axis is orientated along the stator flux vector $\bar{\psi}_{sg}$. For simplicity calculation of the reference current i^*_{sgd} is not shown in this graphic. However, as mentioned before, the current i^*_{sgd} can be used to regulate the reactive power supplied/absorbed by the BDFIG.

3.5. Parameter sensitivity of the proposed control system

The performance of the proposed control system is robust against machine parameter variations. In DFIGs and BDFIGs the orientation of the vector control system is dependent on the correct estimation of the position of the stator flux $\bar{\psi}_{sg}$. This is simple to obtain from (2) using:

$$\bar{\psi}_{sg} = \int (\bar{v}_{sg} - R_{sg}\bar{I}_{sg})dt \rightarrow \theta_{eq} = \tan^{-1}\frac{\psi_{sg\beta}}{\psi_{sg\alpha}} \quad (42)$$

Because the stator of the power machine is connected to the grid voltage (see Fig. 10), the voltage drop in R_{sg} is small and has

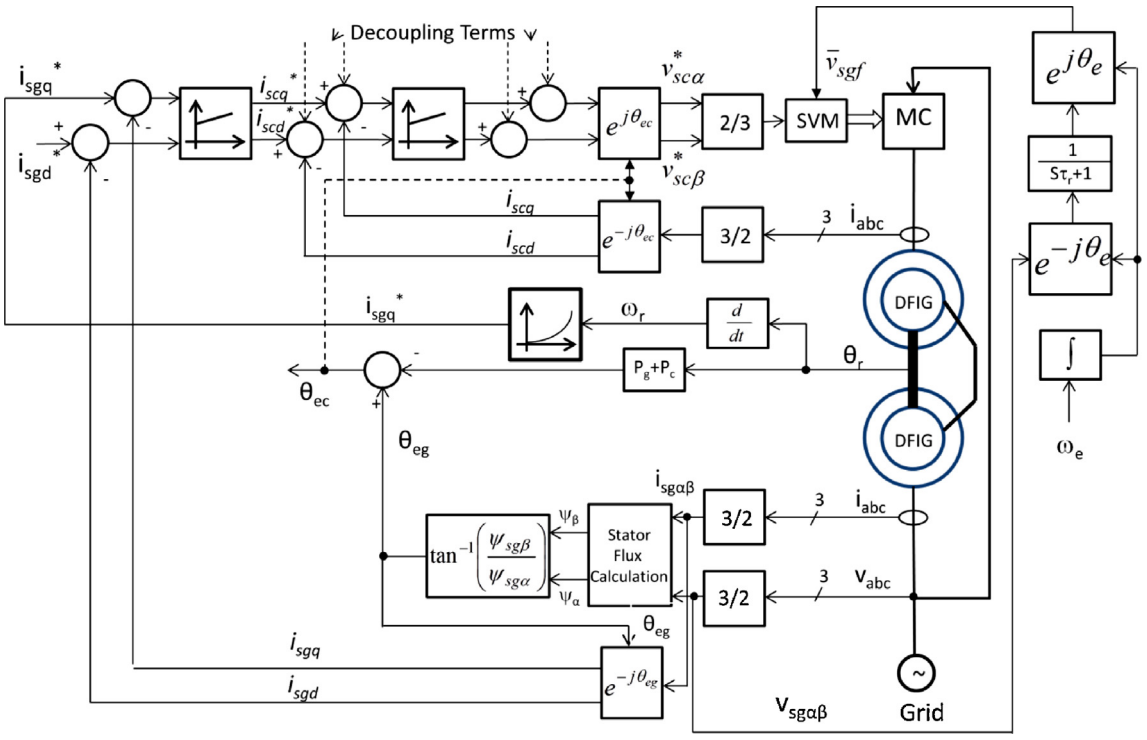

Fig. 10. Vector control system of the proposed generation system. Stator flux orientation is assumed.

a negligible effect in the orientation of the vector control system. Notice that in (42) a modified integrator is usually implemented to avoid the drift produced by dc components in the measured signals (see [37]).

Machine parameter variations can affect the performance of the inner and outer current control loops. However the transfer functions of (20)–(21) are dominated by the large value of ω_{sl} which is about 157 rad s^{-1} for the experimental prototype used in this work. Therefore, large changes in the root locus of Fig. 8 are very unlikely. As discussed above, the transfer function of (41) is robust against variations in ω_{ec} and R_T. Therefore, large variations in the shape of the root locus shown in Fig. 9 are also very unlikely.

4. Control of the matrix converter

The MC is composed of nine bidirectional switches, which can be used to connect any input phase to any output phase of the matrix converter. A 3 × 3 MC is shown in Figs. 1b and 2. The switching matrix can be represented as:

$$\begin{bmatrix} v_a \\ v_b \\ v_c \end{bmatrix} = \begin{bmatrix} S_{11} & S_{12} & S_{13} \\ S_{21} & S_{22} & S_{23} \\ S_{31} & S_{32} & S_{33} \end{bmatrix} \begin{bmatrix} v_A \\ v_B \\ v_C \end{bmatrix} \tag{43}$$

where the switch S_{ij} is located in the row "i" and column "j", as shown in Fig. 2. When $S_{ij} = 0$ the corresponding switch is opened and when $S_{ij} = 1$ the switch is closed. In (43) (A, B, C) are used to denote the input voltages and (a, b, c) are used for the output voltages.

In this work the switches are controlled using the Space Vector Modulation (SVM) algorithm reported in [38]. This method is based on 21 vectors where 18 of them are termed "active vectors" and the remaining 3 are termed "zero vectors". The inputs to the modulation algorithms proposed in [38] are the input voltage $\underline{v}_i$ measured at the filter capacitor (see Figs. 1b and Fig. 11) and the demanded output voltage vector $\underline{v}_0$. The output of the SVM algorithm is used to obtain (during each sampling period) the switching signals for the 9 bidirectional switches of the 3 × 3 MC.

4.1. Modelling of the matrix converter and stability issues

The electrical arrangement of the MC used in this work is shown in Figs. 1b and 11. An LC filter is used in the MC input to improve the waveforms of the current supplied to the grid. Usually a resistor in parallel with the input filter inductance is required to improve the damping of the system. Assuming that the switching frequency is much greater than the input/output fundamental frequencies, the matrix converter can be modelled as an actuator, with the input/output voltages represented by their average values over a cycle period. Therefore the MC input/output relationship is obtained from [38] as:

$$\bar{v}_0 = \frac{3}{2}[\bar{v}_i \bar{m}_i^c + \bar{v}_i^c \bar{m}_d] \tag{44}$$

$$\bar{l}_i = \frac{3}{2}[\bar{l}_0 \bar{m}_i + \bar{l}_0^c \bar{m}_d] \tag{45}$$

where $\bar{v}_i$ and $\bar{v}_0$ are the MC input and output voltage vectors respectively. The superscript "c" is the complex conjugate operator. The vectors $\bar{l}_i$ and $\bar{l}_0$ correspond to the MC input and output current vectors. The demanded values of $\bar{m}_d$ and $\bar{m}_i$ are calculated as: $\bar{m}_d^* = \bar{v}_0^*/(3\bar{v}_i^c)$ and $\bar{m}_i^* = \bar{v}_0^{c*}/(3\bar{v}_i^c)$ (see [26,32,38–40]). As highlighted in [38–40], the input/output relationship of (44)–(45) is applicable even if the MC is not controlled using SVM. The modelling described

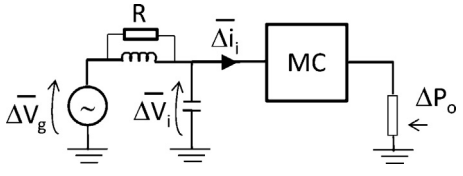

Fig. 11. Single phase diagram of the MC input stage for stability study.

by (44)–(45) is usually applied in the stability studies reported in the literature [39,40].

In a typical application of MCs, the input of the matrix converter is connected to the grid through a second order power filter. The interaction between the input filter, the MC and the load may produce oscillations and even instability at high power operation unless a compensation method is used [39,40]. Using Fig. 9, the incremental impedance ΔZ (at the matrix converter input) is defined as:

$$\Delta Z = \frac{\Delta \bar{v}_i}{\Delta \bar{l}_i} \tag{46}$$

Ideally, the MC outputs are not affected by voltage perturbations at the input, because the modulation algorithm can compensate for them instantaneously by adjusting $\bar{m}_d$ and $\bar{m}_i$ in (44). Therefore if the losses are neglected, the MC input/output power can be considered constant ($\Delta P_o = 0$) and the incremental impedance of (46) can have a relatively low negative real component reducing the damping coefficient of the MC input stage. This negative "resistance" is produced because positive variations in $\Delta \bar{v}_i$ produce negative variations in $\Delta \bar{l}_i$ and vice versa. A complete discussion of this issue is presented in [41].

In this work the stability of the matrix converter is improved by using a first order filter implemented in a synchronously rotating reference frame [40,41]. The voltages are referred to a d–q axis rotating at the synchronous velocity:

$$v_{id} + jv_{iq} = (v_{i\alpha} + jv_{i\beta})e^{-j\theta_e} \tag{47}$$

Therefore the voltages v_{id}, v_{iq} are dc values. The high frequency components are filtered-out using

$$v_{ifd} = \frac{v_{id}}{s\tau_f + 1} \quad v_{ifq} = \frac{v_{iq}}{s\tau_f + 1} \tag{48}$$

and are then transformed again to the stationary α–β axis using:

$$v_{if\alpha} + jv_{if\beta} = (v_{ifd} + jv_{ifq})e^{j\theta_e} \tag{49}$$

The synchronous filter has the advantage of not producing any phase shift at the fundamental frequency of the input voltage even if a narrow low pass filter is used in (48). The values of $v_{if\alpha}$, $v_{if\beta}$ are used in the modulation algorithm (i.e. for the calculation of $\bar{m}_d^*$ and $\bar{m}_i^*$) and the stability is improved by increasing the value of the incremental impedance of (46). For instance if a very narrow low-pass filter is used, i.e. $\tau_f \to \infty$, then $\Delta \bar{l}_i = 0$ for any $\Delta \bar{v}_i$ and $\Delta Z \to \infty$. In this case the damping coefficient of the output stage is not changed. However, a very large value of τ_f cannot be used in (48), because the voltage perturbations cannot be completely rejected by the SVM algorithm [39–41].

In this work a synchronous filter with a cut-off frequency of 50 Hz is used in the experimental system. This value is adequate to produce good dynamic response in the whole operating range.

5. Experimental results

A prototype of the brushless generating system of Fig. 1, was implemented using two 4-pole Doubly-Fed Induction Machines. The experimental system arrangement is shown in Figs. 12 and 13. A third cage machine is used to drive the proposed generation system. This machine is speed-controlled by a commercial inverter. Using the emulation technique discussed in [26], the cage induction machine is controlled to emulate a variable speed wind turbine or a diesel engine.

As shown in Fig. 12, in the experimental system the rotor current, two stator currents, the grid voltage, the rotational speed and the matrix converter input voltage are measured. However the rotor currents are measured only for comparison purposes. In some applications additional inductances are not required to implement

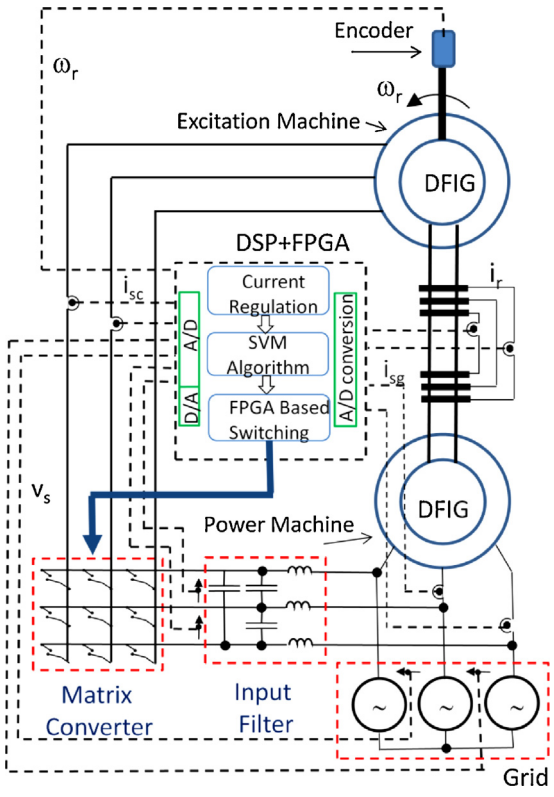

Fig. 12. Brushless generating system proposed.

the matrix converter input filter, because the inductances of the grid and DFIG are sufficient to reduce the harmonic distortion in the MC input current [32]. In this case the matrix converter input voltage vector and the grid voltage vector are identical and transducers to measure only one of them are required in the implementation shown in Fig. 12.

The space vector modulation algorithm required for the matrix converter and the control system of Figs. 6 and 10 are implemented using a DSP based control board and an FPGA, the latter implementing a four-step current commutation method [33] and generating the switching signals for the IGBT gate drivers. The MC and the grid-connected DFIG are connected to a three-phase variable transformer at the input. For data acquisition purposes an external board,

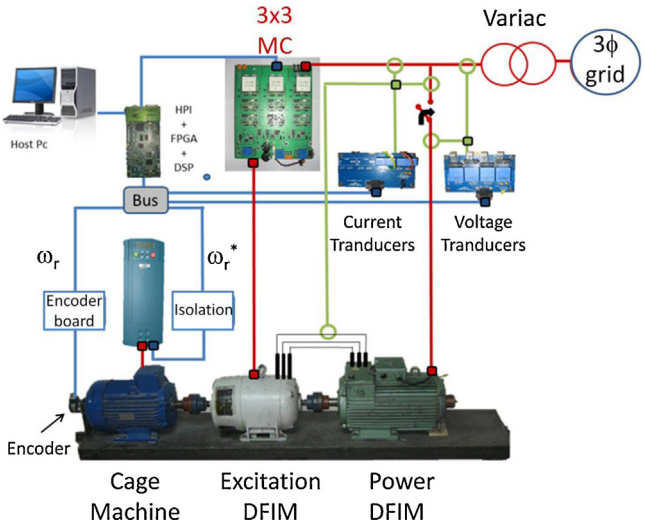

Fig. 13. Implementation of the experimental system corresponding to Fig. 12.

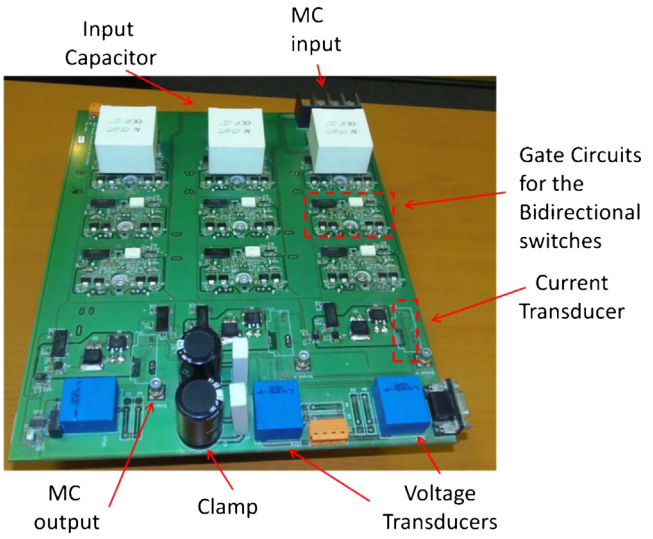

Fig. 14. 3 × 3 matrix converter prototype used in this work.

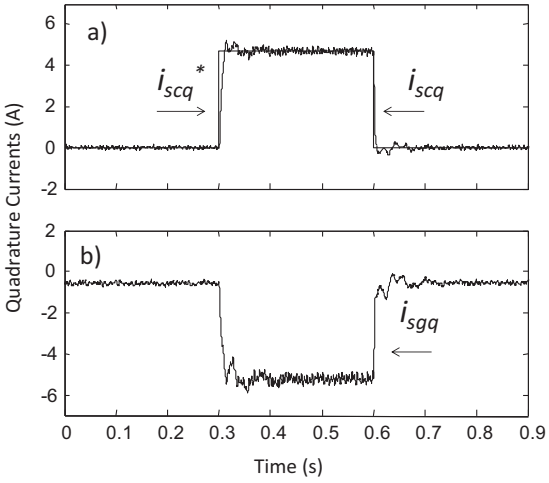

Fig. 16. Control system response for a change in the quadrature current i_{scq}. (a) Step variation in i_{scq} and (b) corresponding variation in i_{sgq}.

with ten 14bit Analogue to Digital (ADC) channels each with 1 μs conversion time, is interfaced to the DSP. This board also has 4 Digital to Analogue (DAC) channels available. Hall-effect transducers are used to measure the input currents, input voltages and output currents (see Figs. 12 and 13). A position encoder of 10000ppr is used to measure the rotor position angle. Sensorless operation of the BDFIG is also feasible by adapting some of the sensorless methods typically used with a conventional DFIM.

Fig. 14 shows the MC prototype used in this work. The MC was designed by the Power Electronic Machines and Control Group (PEMC) at the University of Nottingham and uses Semikron SK60GM123 bidirectional switches. The PCB board includes clamp circuits and current/voltage transducers. Unless otherwise stated, the sampling time used by the modulation and control algorithms is 80 μs.

In Fig. 15, the control system response of the internal current control loop is shown. The system is operating at about 980 rpm (i.e. $s_T = 30\%$, see (39)), with the torque current i_{scq} and magnetising current i_{scd} initially regulated to zero. At $t \approx 0.3$ s the reference magnetising current i_{scd} is changed to ≈4.8 A (rms). For this test the currents i_{sgd} and i_{sgq} are not regulated.

In Fig. 15a, the control system response for the inner loop is shown. A zoomed view of Fig. 15a is also shown in Fig. 15b. The performance of the control system is good with a settling time of less than 10 ms. Fig. 15c shows the direct axis current in the stator connected to the grid. Before the step the currents required to magnetise the machines are taken from the grid. After the step the machines are magnetised from the excitation DFIM and the current i_{sgd} becomes positive, i.e. reactive power is supplied to the grid.

The performance of the i_{scq} control loop has also been tested and the results shown in Fig. 16. Again the rotational speed is about 980 rpm. At $t \approx 0.3$ s, the torque current in the excitation machine is changed from 0 to about 4.8 A (rms). The performance of the quadrature current control loop is similar to that depicted in Fig. 15a and b. The settling time is ≈10 ms and the step change in i_{scq} produces a corresponding change in the torque current i_{sgq}. Fig. 17 shows the instantaneous currents corresponding to the test of Fig. 16. The stator current of the excitation machine is shown

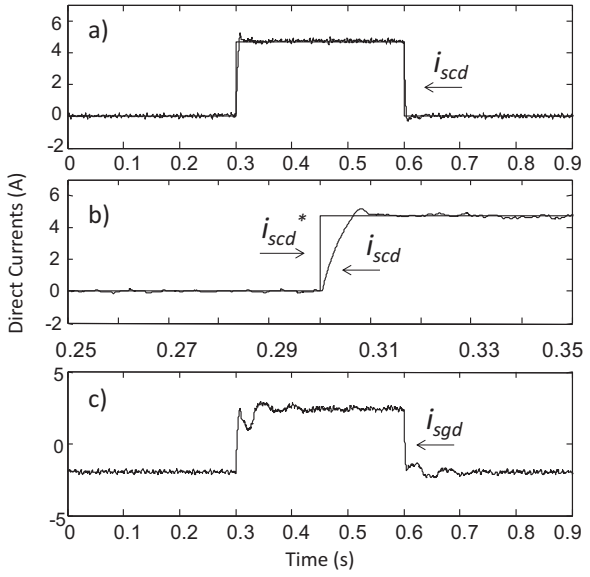

Fig. 15. Control system response for a step change in the magnetising current. (a) Step change in i_{scd}^*, (b) a zoomed view of Fig. 15a and (c) direct axis current of the DFIG connected to the grid.

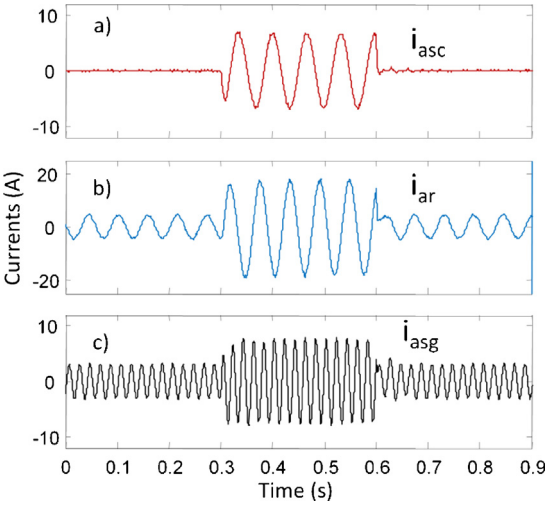

Fig. 17. Instantaneous currents corresponding to a test similar to that of Fig. 16. (a) Stator current in the excitation machine, (b) rotor current and (c) stator current in the power machine.

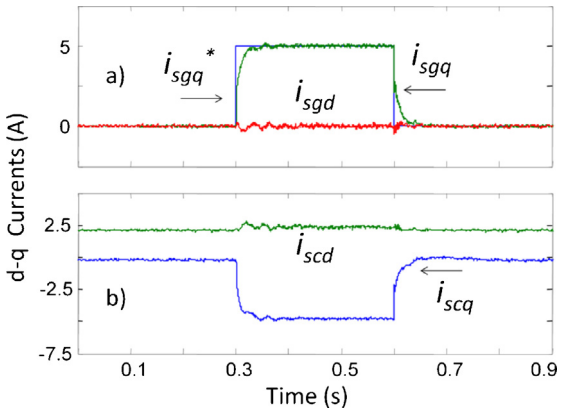

Fig. 18. Performance of both control loops. (a) Control system response for a step change in the current i_{sgq} and (b) control system response for the internal control loop for i_{scq}.

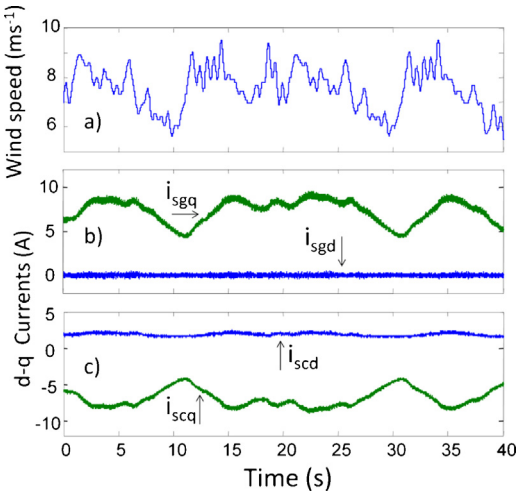

Fig. 20. Performance of the system considering the emulation of a variable speed wind turbine. (a) Wind profile and (b) currents in the stator of the power DFIM and (c) current in the stator of the excitation machine.

in Fig. 17a (a signal of about 15 Hz), the rotor current is shown in Fig. 17b (a signal of about 17 Hz) and the 50 Hz current i_{sgq} is shown in Fig. 17c. Notice that the current supplied to the stator of the excitation machine is well regulated and has little distortion.

The performance of both control loops is shown in Fig. 18. The machine is operating at ≈525 rpm (s_T in (39) is ≈ −30%) when a step change in i_{sgq}^* is applied at $t \approx 0.3$ s. The settling time for i_{sgq} is about 60 ms which is considered appropriate for this application. No overshoot is produced in the i_{sgq} current, which validates the root locus analysis of Fig. 8, and the discussion of Section 3.3.

As shown in Fig. 18b the machines are fully magnetised from the excitation side. Notice that there is some cross-coupling between the d- axis and q-axis components (see (19)–(21)). After the load step in i_{sgq} there are some minor oscillations in the d component of the currents.

The proposed system has also been tested considering a ramp speed variation between approximately 620 rpm to 920 rpm. The outer control system is regulated for $i_{sgq} \approx 5$ A and $i_{sgd} \approx 0$. The stator of the power DFIM is connected to a 110 V neutral to phase 3ϕ balanced grid.

The performance of the system, considering a ramp speed variation is shown in Fig. 19. In Fig. 19a the rotational speed ω_r is depicted. The commercial inverter is controlled using one of the D/A

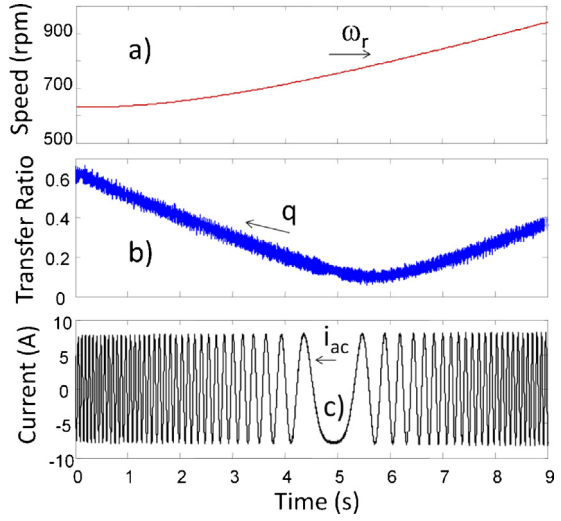

Fig. 19. Performance of the system considering a ramp variation in the rotational speed. (a) Rotational speed and (b) voltage transfer ratio q and (c) stator current in the excitation DFIM.

outputs to set the reference speed for the cage machine. Fig. 19b shows the voltage transfer ratio of the matrix converter which is calculated as $q = (|\bar{v}_0|/|\bar{v}_i|)$. As the rotational speed is approaching $\omega_r \approx 750$ rpm (i.e. $s_T \approx 0$), the signals applied to the stator of the excitation machine have a frequency close to ≈0 Hz and the matrix converter output voltage is small because the back-emf of (28) is also small.

Fig. 19c shows the current in the stator of the excitation machine. Notice that close to 750 rpm, i.e. $\omega_{ec} \approx 0$, the current i_{ac} changes its phase. This is similar to the behaviour of the rotor current of a conventional DFIG, when the machine is going through the synchronous speed.

To test the performance of the proposed brushless generation system for wind energy applications, a 3 kW wind turbine is emulated using the methodology discussed in [26]. Fig. 20a shows the wind profile used in this emulation which has speed variations between 5.5 ms^{-1} and 9.5 ms^{-1}. The wind-profile of Fig. 20a is sampled each 0.1 s and sent to the DSP, where a mathematical model of the WECS is implemented. The rotational speed of the wind turbine is calculated from this model and sent to the commercial inverter which controls the cage machine driving the proposed generation system.

Fig. 20b shows the d–q axis stator currents of the power DFIG. For this test the machines are magnetised from the excitation DFIM and the current $i_{sgd}^* = 0$. The reference current i_{sgq}^* is regulated in order to drive the WECS to the point of maximum aerodynamic efficiency (see (34)–(36)). Fig. 20c shows the d–q axis stator currents corresponding to the excitation machine. As shown by (20) the quadrature currents in the stators are in anti-phase.

The magnetising current in the excitation machine is also shown in Fig. 20c. Notice that i_{scd} has some low frequency oscillations correlated with the rotational speed (see Fig. 21c). This is due to the fact that the stator flux (see (16)) is also dependent on the torque currents i_{scq} and i_{sgq}.

Fig. 21 shows the output power, the voltage transfer ratio and the rotational speed corresponding to the test of Fig. 20. As expected from (34), the rotational speed and the output power are correlated. The voltage transfer ratio is shown in Fig. 21b. As mentioned before, the voltage transfer ratio is dependent on the back-emf value. Therefore, when the frequency is close to ≈0 Hz, the voltage transfer ratio q becomes low.

Tracking of the point of maximum aerodynamic efficiency is shown in Fig. 21c. The dotted line shows the optimal rotational

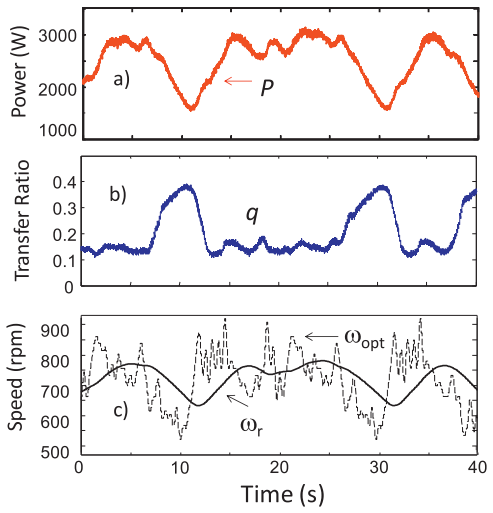

Fig. 21. Power, voltage transfer ratio and rotational speed corresponding to the test of Fig. 20. (a) Output power, (b) voltage transfer ratio q and (c) rotational speed and optimal speed.

speed ω_{opt} which, for a given wind turbine, is proportional to the wind velocity. The solid line shows the rotational speed of the BDFIG. As expected the inertia of the energy system acts as a low pass filter, filtering out the high frequency components of ω_{opt}. The inertia of a Wind Energy Conversion System is usually relatively high and does not allow perfect tracking of fast fluctuations in the optimal rotational speed. A discussion of the effects of inertia for tracking of the optimal speed ω_{opt} is presented in [42].

6. Conclusions

In this paper a brushless DFIG has been presented and the mathematical model has been derived. A control system based on two nested loops has been presented. An inner faster loop is used to regulate the stator current of the control DFIG. A slower external loop is used to regulate the active and reactive power supplied to the grid. This topology is appropriate for wind energy applications, considering that the power spectrum density of a typical wind profile has most of the available energy in the low frequency region.

Experimental results have been presented in this paper; the system has been tested for step variations in the control current, grid current, wind profiles and ramp variations in the rotational speed. For all the experimental tests the performance of the proposed BDFIG has been very good.

The topology presented in this system is based on a 3×3 matrix converter. The experimental results discussed in this paper show that the matrix converter has a good and stable performance for this application.

Acknowledgements

This work was funded by Fondecyt Chile under Contracts 1110984 and 1121104. The financial support of Fondequip Chile, project EQM12011, and CONICYT/FONDAP/15110019 is also acknowledged.

Appendix.

A.1. Parameters of the experimental system

Parameters referred to the stator of the excitation DFIM

$R_{sc} = 2.54\Omega \quad R_r = 5.29\Omega \quad R_{sg} = 2.75\Omega$

$L_{sc} = 0.19H \quad \mathrm{L_r} = 0.65\mathrm{H} \quad \mathrm{L_{sg}} = 0.46\mathrm{H}$

$L_{0g} = 0.44H \quad L_{0c} = 0.18H$

A.2. Machines used in the experimental system

	Power DFIM	
Poles = 4	Nominal i_r = 15 A (rms)	Power = 4 kW
Nominal V_s = 380 V	Nominal i_s = 15 A	
	Excitation DFIM	
Poles = 4	Nominal i_r = 11 A (rms)	Power = 2.5 kW
Nominal V_s = 380 V	Nominal i_s = 5 A	

References

[1] M. Liserre, R. Cárdenas, M. Molinas, J. Rodríguez, Overview of multi-MW wind turbines and wind parks, IEEE Transactions on Industrial Electronics 58 (2011) 1081–1095.
[2] L. Xu, B. Guan, H. Liu, L. Gao, K. Tsai, Design and control of a high-efficiency Doubly-Fed Brushless machine for wind power generator application, in: 2010 IEEE Energ. Conver. Congress and Expo. (ECCE), 2010, pp. 2409–2416.
[3] T. Logan, J. Warrington, S. Shao, R. McMahon, Practical deployment of the Brushless Doubly-Fed Machine in a medium scale wind turbine, in: Int. Conf. on Power Electr. and Drive Systems, 2009 (PEDS 2009), 2009, pp. 470–475.
[4] S. Shao, E. Abdi, R. McMahon, Vector control of the Brushless Doubly-Fed Machine for wind power generation, in: IEEE Int. Conf. on Susta Energ. Techno. 2008 (ICSET 2008), 2008, pp. 322–327.
[5] L.J. Hunt, A new type of induction motor, Journal of the Institute of Electrical Engineers 39 (1907) 648–667.
[6] L.J. Hunt, The cascade induction motor, Journal of the Institute of Electrical Engineers 52 (1914) 406–426.
[7] F. Creedy, Some developments in multispeed cascade induction motors, Journal of IEE (London) 59 (1927) 511–532.
[8] B.H. Smith, Synchronous behavior of doubly fed twin stator induction, IEEE Transactions on Power Apparatus and Systems 86 (1967) 1227–1234.
[9] A.R.W. Broadway, L. Burbridge, Self-cascaded machine: a low-speed motor or high-frequency brushless alternator, in: Proceedings of the Institute of Electrical Engineers, 117, 1970, pp. 1277–1290.
[10] B. Hopfensperger, D.J. Atkinson, Doubly-fed a.c.machines: classification and comparison, in: Proc. of the 9th Euro. Conf. on Power Electr. and Appl., 2001.
[11] B. Hopfensperger, D.J. Atkinson, R.A. Lakin, Stator-flux oriented control of a doubly-fed induction machine without position encoder, in: IEE Proceedings – Electric Power Applications, 147, 2000, pp. 241–250.
[12] B. Hopfensperger, D.J. Atkinson, R.A. Lakin, Stator flux oriented control of a cascaded doubly-fed induction machine, in: IEE Proceedings – Electric Power Applications, 146, 1999, pp. 597–605.
[13] B. Hopfensperger, D.J. Atkinson, R.A. Lakin, Combined magnetising flux oriented control of the cascaded doubly-fed induction machine, in: IEE Proceedings – Electric Power Applications, 148, 2001, pp. 354–362.
[14] P. Rochelle, R. Spee, A.K. Wallace, The effect of stator winding configuration on the performance of brushless doubly-fed machines in adjustable speed drives, in: Conf. Record of the 1990 IEEE Ind. Appl. Society Annual Meeting, 1990, 1, 1990, pp. 331–337.
[15] A.K. Wallace, R. Spee, G.C. Alexander, The brushless doubly-fed machine: its advantages, applications and design methods, in: Sixth Int. Conf. on Electr. Mach. and Drives, 1993. (Conf. Publ. No. 376), 1993, 1993, pp. 511–517.
[16] P.C. Roberts, R.A. McMahon, P.J. Tavner, J.M. Maciejowski, T.J. Flack, Equivalent circuit for the brushless doubly fed machine (BDFM) including parameter estimation and experimental verification, in: IEE Proceedings – Electric Power Applications, 152, 2005, pp. 933–942.
[17] X. Wang, R.A. McMahon, P.J. Tavner, Design of the Brushless Doubly-Fed (Induction) machine, in: IEEE Int. Electr. Mach. & Drives Conf., 2007 (IEMDC'07), 2007, pp. 1508–1513.
[18] F. Barati, S. Shao, E. Abdi, H. Oraee, R. McMahon, Generalized vector model for the Brushless Doubly-Fed machine with a nested-loop rotor, IEEE Transactions on Industrial Electronics 58 (2011) 2313–2321.
[19] F. Barati, H. Oraee, E. Abdi, S. Shao, R. McMahon, The Brushless Doubly-Fed machine vector model in the rotor flux oriented reference frame, in: 34th Annual Conf. IEEE Ind.l Electr., 2008 (IECON 2008), 2008, pp. 1415–1420.

[20] J. Poza, E. Oyarbide, I. Sarasola, M. Rodriguez, Vector control design and experimental evaluation for the brushless doubly fed machine, IET Electric Power Applications 3 (2009) 247–256.
[21] J. Poza, E. Oyarbide, D. Roye, M. Rodriguez, Unified reference frame *dq* model of the brushless doubly fed machine, IEE Proceedings – Electric Power Applications 153 (2006) 726–734.
[22] S. Shao, E. Abdi, F. Barati, R. McMahon, Stator-flux-oriented vector control for Brushless Doubly Fed Induction Generator, IEEE Transactions on Industrial Electronics 56 (2009) 4220–4228.
[23] T. Long, S. Shao, T. Logan, R. McMahon, A novel vector control approach for single phase Brushless Doubly Fed Machine, in: 37th Annual Conference on IEEE Ind. Electr. (IECON 2011), 2011, pp. 1722–1727.
[24] A. Sureda, A. Munoz, R. Pena, R. Cardenas, J. Clare, P. Wheeler, Control of a Brushless Doubly-Fed induction generator via a matrix converter, in: Proc. of the 2011 – 14th Europ. Conf. on Power Electr. and Appl. (EPE 2011), 2011, pp. 1–9.
[25] N. Patin, E. Monmasson, J.-P. Louis, Modeling and control of a cascaded doubly fed induction generator dedicated to isolated grids, IEEE Transactions on Industrial Electronics 56 (2009) 4207–4219.
[26] R. Cardenas, R. Pena, J. Clare, P. Wheeler, Analytical and experimental evaluation of a WECS based on a Doubly Fed Induction Generator fed by a matrix converter, IEEE Transactions on Energy Conversion 26 (2011) 204–215.
[27] R. Pena, R. Cardenas, E. Reyes, J. Clare, P. Wheeler, Control of a Doubly Fed Induction Generator via an indirect matrix converter with changing DC voltage, IEEE Transactions on Industrial Electronics 58 (2011) 4664–4674.
[28] K. Protsenko, X. Dewei, Modeling and control of Brushless Doubly-Fed Induction Generators in wind energy applications, IEEE Transactions on Power Electronics 23 (2008) 1191–1197.
[29] P. Kostyantyn, X. Dewei, Modeling and control of Brushless Doubly-Fed Induction Generators in wind energy applications, in: Twenty Second Annual IEEE Applied Power Electronics Conference (APEC 2007), 2007, pp. 529–535.
[30] H. Voltolini, R. Carlson, Grid synchronization and maximum power point tracking for wind energy generation system with Brushless Doubly Fed Induction Generator, in: IECON Ind. Electr., 2008, 2008, pp. 2173–2177.
[31] M. Boger, A. Wallace, Performance capability analysis of the brushless doubly-fed machine as a wind generator, in: Seventh Int. Conf. on Electr. Mach. and Drives, 1995. (Conf. Publ. No. 412), 1995, pp. 458–461.
[32] R. Cardenas, R. Pena, J. Clare, P. Wheeler, Analytical and experimental evaluation of a WECS based on a Cage Induction Generator Fed by a matrix converter, IEEE Transactions on Energy Conversion 26 (2011) 204–215.
[33] P.W. Wheeler, J.C. Clare, L. Empringham, M. Bland, K.G. Kerris, Matrix converters, IEEE Industry Applications Magazine 10 (2004) 59–65.
[34] R. Pena, R. Cardenas, E. Reyes, J. Clare, P. Wheeler, A topology for multiple generation system with Doubly Fed Induction Machines and indirect matrix converter, IEEE Transactions on Industrial Electronics 56 (2009) 4181–4193.
[35] T. Friedli, J. Kolar, J. Rodriguez, P. Wheeler, Comparative evaluation of three-phase AC–AC matrix converter and voltage DC-link back-to-back converter systems, IEEE Transactions on Industrial Electronics (2011) 1.
[36] T.F. Podlesak, D.C. Katsis, P.W. Wheeler, J.C. Clare, L. Empringham, M. Bland, A 150-kVA vector-controlled matrix converter induction motor drive, IEEE Transactions on Industry Applications 41 (2005) 841–847.
[37] R. Pena, J.C. Clare, G.M. Asher, Doubly fed induction generator using back-to-back PWM converters and its application to variable-speed wind-energy generation, IEE Proceedings – Electric Power Applications 143 (1996) 231–241.
[38] D. Casadei, G. Serra, A. Tani, L. Zarri, Matrix converter modulation strategies: a new general approach based on space-vector representation of the switch state, IEEE Transactions on Industrial Electronics 49 (2002) 370–381.
[39] D. Casadei, G. Serra, A. Tani, A. Trentin, L. Zarri, Theoretical and experimental investigation on the stability of matrix converters, IEEE Transactions on Industrial Electronics 52 (2005) 1409–1417.
[40] D. Casadei, J. Clare, L. Empringham, G. Serra, A. Tani, A. Trentin, P. Wheeler, L. Zarri, Large-signal model for the stability analysis of matrix converters, IEEE Transactions on Industrial Electronics 54 (2007) 939–950.
[41] R. Caĭrdenas, R. Peña, J. Clare, P. Wheeler, Analytical and experimental evaluation of a WECS based on a cage induction generator fed by a matrix converter, IEEE Transactions on Energy Conversion 26 (2011) 204–215.
[42] E. Echenique, J. Dixon, R. Cardenas, et al., Sensorless control for a switched reluctance wind generator, based on current slopes and neural networks, IEEE Transactions on Industrial Electronics 56 (2009) 817–825.